Hierarchically organized biomimetic architectured silk fibroin-ceramic based anisotropic hybrid aerogels for thermal energy management

Hajar Maleki[1,*], Thomas Fischer[1], Christoph Bohr[1], Jaqueline Auer[2], Sanjay Mathur[1], Barbara Milow[1,3]

[1]Institute of Inorganic Chemistry, Department of Chemistry, University of Cologne, Greinstraße 6, 50939 Cologne, Germany

[2] University of Applied Sciences Upper Austria, Stelzhamerstraße 23, 4600 Wels, Austria

[3]Department of Aerogels and Aerogel Composites, Institute of Materials Research, German Aerospace Center (DLR), Linder Höhe, 51147 Cologne, Germany

E-mail: h.maleki@uni-koeln.de

TOC
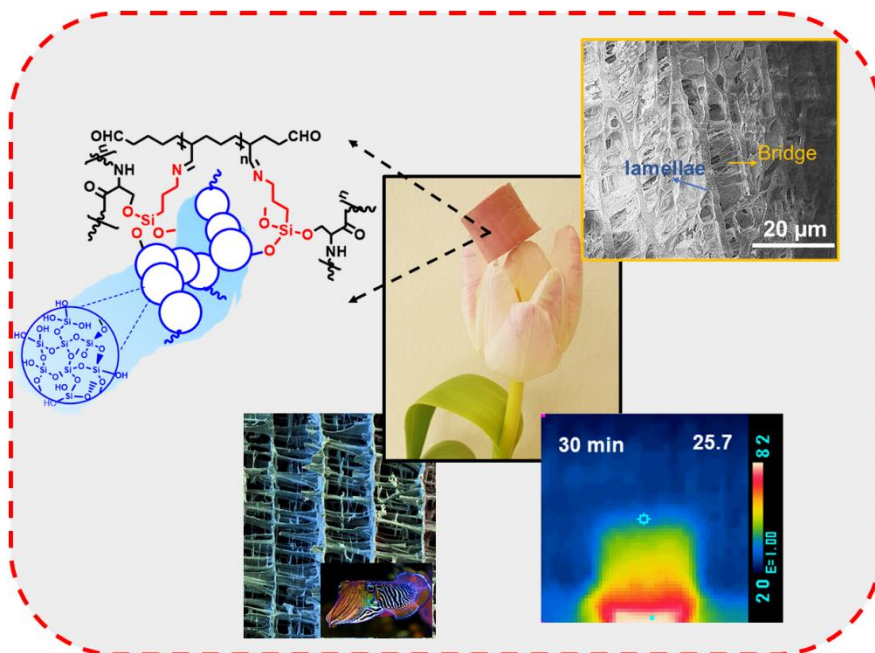
Abstract

Due to the current energy crises, the search for thermal energy management systems based on thermal insulating porous materials has drawn a significant deal of attention. Herein, we demonstrated the thermal insulation and management capabilities of cuttlefish bone mimetic aerogels with hierarchically organized porous structures directly fabricated from surface modified and self-assembled silk fibroin biopolymer extracted from *b. Mori* silkworm cocoon biomass hereafter, the materials developed referred to as X-*AeroSF*. Exploiting from creating an interpenetrating network of the secondary ceramic components of various one, two, and three-dimensional sepiolite ($Mg_2H_2Si_3O_9.xH_2O$), MXene ($Ti_3C_2T_X$) and silica nanostructures inside the self-assembled silk fibroin biopolymer and subsequent uni-directional freeze-casting and drying the resulted hydrogels, composites with aerogel feature were obtained. The obtained aerogels possess low bulk density (ρ_b = 0.059-0.090 g cm^{-3}), low thermal conductivities (λ = 0.035-0.042 W m^{-1} K^{-1}), and high thermal stability (up to ~ 260 °C) with multi-modal lamella-bridge porous microstructures found in the cuttlefish bone structure. In addition, the intriguing anisotropy in the X-*AeroSF* composites porous structure enables thermal dissipation along with the aligned pore directions, thus decreasing the local overheating on the heated side. As a result, an improvement in thermal insulation in the perpendicular direction with respect to the pore lamellae was obtained. Therefore, the exquisite thermal energy management, biodegradability, low bulk density, fire resistivity, together with possible manufacture scalability of X-*AeroSF* composite, make this material attractive for future practical applications.

Keywords: Aerogels, bioinspired materials, thermal energy management, thermal insulation, composites

1. Introduction

Due to the rising global demands for energy efficiency, designing high-performance thermally insulating materials for thermal energy management has drawn significant attention. Considering that thermal energy production causes a high release of carbon emission, thermal energy management is vitally required to save energy and reduce its carbon footprint[1]. In this regard, many efforts have been made to develop a new set of materials and structures that possess desired thermal conductivities and thermal energy management possibilities in electronics, buildings, energy storage, conversation systems, among others[2]. As well-studied versatile porous materials, aerogels[3, 4] considered for a wide range of applications in a multitude of areas such as thermal insulation, pollution abatement, catalysts and catalyst supports, mechanical damping, thanks to their ultra-low density, low thermal conductivity, high-energy absorption, and so on[4]. Numerous efforts have hitherto been made to fabricate thermally super-insulating aerogels with thermal conductivities below 0.02 W m^{-1}K^{-1} from purely ceramics, polymeric and hybrid aerogels[5, 6, 7, 8, 9, 10] Nevertheless, research on the anisotropic aerogels to control the heat transfer in a certain direction while lowering the heat localization in the materials for the purpose of energy management is nowadays drawing more interest. One important example in this regard is thermal energy management in the miniaturized electronic devices by removing the heat generated during device operation to increase their lifetime and efficiency[11,12].

While traditional biopolymeric aerogels[13] have been vastly developed in recent years, their low mechanical strength, poor resistance to the fire, and high moisture sensitivity are still significant challenges to mitigate. In addition, from a microstructural point of view, most of these aerogels reported hitherto are isotropic, which is not sufficient for thermal energy management purposes in their pristine forms[14]. Thus, the development of aerogels with anisotropic microstructure with precise control on the pore orientation and microstructure is still a great challenge and could be an intriguing strategy for thermal energy management purposes[15, 14, 16].

Silk fibroin (SF) is a naturally occurring fibrous protein-based biopolymer extracted from *b. Mori* silkworm cocoon and has been vastly exploited for the processing of various intriguing functional materials, including aerogels[17]. The SF biopolymer aerogels, so-called *AeroSF*, are quite a new category of biopolymeric aerogels with an ultra-low thermal conductivity that have been very recently reported by our group.[18, 19, 20] . Thanks to its nanoporosity originated from controlled self-assembly and subsequent entanglement of the polymer chains in the nanoscale, *AeroSF* has indicated interesting thermal insulation properties with thermal conductivity values of *ca.* 0.019 W m^{-1} K^{-1}, and compressibility up to 80% of strain and ultra-low bulk density (0.02 g cm^{-3})[19].

However, a multitude of improvements on some properties like mechanical strength and toughness, further control on the microstructure, is still necessary to render the *AeroSF* promising for thermal insulation and thermal energy management applications. In this work, we structurally designed a series of anisotropic and bioinspired SF based aerogel hybrids through a robust cross-linking of SF with glutaraldehyde (GA) as an organic cross-linker (X-*AeroSF*) and further hybridization of the resulted structures with several secondary inorganic nano-additives of three, two and one dimensional (3D, 2D, and 1D) ceramics such as silica, titanium carbide nanosheets (NSs) (MXene, $Ti_3C_2T_X$, T_X: -OH, -F, -O,) [21], and sepiolite (SEP, $Mg_2H_2Si_3O_9.xH_2O$) porous nanorods[22] as the secondary inorganic phases (*cf.* Fig. 1). While cross-linking of SF with GA increased the mechanical toughness in the *AeroSF*, incorporation of the secondary silica (3D), MXene (2D), and SEP (1D) ceramic nanostructures is particularly appealing as they are not only known for reducing the solid heat conduction due to their phonon scattering[23] but also confer heat resistivity to the designed final aerogel composites[15]. Final implementation of bioinspired uni-directional ice templating approach[24, 25] on the as-synthesized hybrid hydrogels, control the microstructural alignment, and pore channel morphologies to lamella and lamella-bridge microstructures resembling the bone structure in the cuttlefish. Meanwhile, due to the large aspect ratio and nano-dispersibility, SEP nanorods and MXene 2D nanostructures are intertwined with SF biopolymer to form composite aggregates with good structural stability. The image of developed anisotropic aerogel composites of this study with varying the ceramic part and with their proposed chemical structures are presented in Fig. 1.
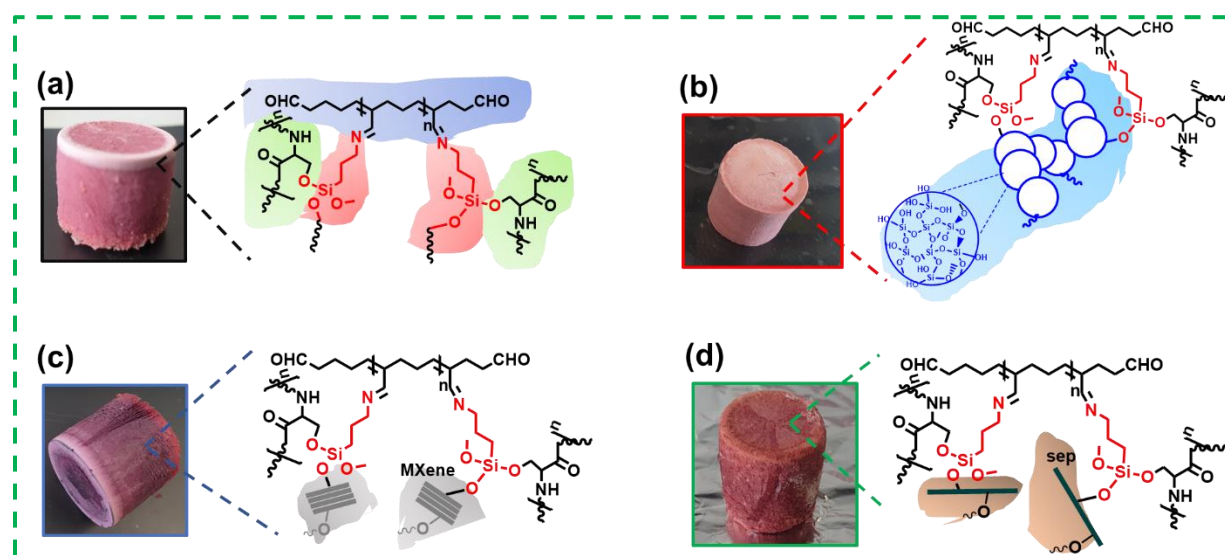

Figure 1. The aerogel composites of this study with their proposed chemical structures. (a) *X-AeroSF*, (b) Silica3-SilSF-GA-6, (c) MXene0.1-SilSF-GA-6, and (d) SEP0.1-SilSF-GA-6.

Accordingly, in this study, microstructural orientation and heat resistivity, but also desired heat transfer performance in the final aerogels were successfully controlled by considering the following aspects. (1) Chemical cross-linking of SF with GA could enhance the structural and chemical stability in the previously developed *AeroSF*. (2) The incorporation of inorganic nanostructures could improve the interfacial dispersion in the composite and the heat resistance in the final hybrid aerogel. (3) Only through a precisely controlled uni-directional freeze casting strategy, anisotropic aerogels with interesting bioinspired pore micro-morphologies have been obtained for the next generation of the aerogels with a possibility of thermal energy management. The developed aerogel structures were studied in terms of surface chemistry, and microstructure mainly pores micromorphology and structural alignment, thermal stabilities, and anisotropic heat transfer behavior and correlated with synthesis and processing parameters. Finally, the proposed anisotropic and biomimetic aerogel composites developed in this study are expected to act as emerging sustainable aerogels for thermal energy management.

2. Methods

2.1. Synthesis

Materials. All chemicals in this study were used without purification. The Bombyx mori silkworm cocoons were purchased from Wild Fibers, U.K. Tetraethyl orthosilicate (98% purity, TEOS), hexadecyltrimethylammonium bromide (98% purity, CTAB), amino propyltriethoxysilane (APTES, 99%), ethanol (99.9%, EtOH), calcium chloride (99.99% purity, $CaCl_2$), sodium carbonate (Na_2CO_3), glutaraldehyde (50% in water), and sepiolite ($Mg_4Si_6O_{15}(OH)_2 \cdot 6H_2O$) were received from Sigma-Aldrich. SnakeSkin ™ dialysis tubing with molecular weight cutoffs of 3.5 kDa was purchased from ThermoFisher Scientific. Titanium aluminum carbide powder (Ti_3AlC_2, 99% purity) was purchased from Nanoshel. The lithium fluoride (LiF, 98%) was purchased from Alfa Aesar.

2.1.1. Silk fibroin extraction. The SF aqueous solution was extracted from silkworm cocoons through a slightly modified procedure reported by Zheng *et al.*[26] First, silk cocoons (5 g) were cut into dime-sized pieces and boiled for 30 min in a 2 L solution of Na_2CO_3 (0.02 M); then, fibers were rinsed with plenty of distilled water and dried overnight. 4 g degummed silk fibers were dissolved in 20 mL of (Ajisawa's reagent, $CaCl_2$/EtOH/water molar ratio of 1:2:8) at 80 °C for 2 h. The solution was dialyzed continuously to remove chemical compounds ($CaCl_2$ and ethanol) dialyzed against distilled water for 48 h. The dialyzed SF solution was centrifuged twice at 9000 rpm, and the supernatant was stored at 4 °C for later use.

2.1.2. Synthesis of $Ti_3C_2T_x$. The MXene nanosheet was synthesized by the etching method, which is reported by M. Alhabeb *et al.*[21]. The MAX phase, Ti_3AlC_2 powder (1 g) was slowly added into

the 20 mL of 9 M hydrochloric acid (HCl, technical grade, 35−38%), followed by slow addition of 1 g of lithium fluoride to the mixture solution and allowing the etching of the Al layer at 35 °C for 24 h. The acidic supernatant was removed by repeated centrifugation process (approximately 8 - 10 times) to finally obtain a stable dark green supernatant of $Ti_3C_2T_x$ with a pH of ~ 6. The concentration of the MXene solution was quantified by drying at 40 °C in an oven and weighing the MXene film.

2.1.3. Fabrication of Silica, MXene, Sepiolite – glutaraldehyde modified silk fibroin based aerogels. The detailed formulations of the aerogel composites of the current study are listed in Table 1. According to Table 1, four different formulations were synthesized, namely *X-AeroSF*, Silica**x**-SilSF-GA-**y**, SEP**x**-SilSF-GA-**y**, MXene**x**-SilSF-GA-**y**, where **x** refers to the mass fraction of the used ceramics with respect to the SilSF in the sol and **y** refers to the GA content in the aerogel composites. With varying the glutaraldehyde and ceramic contents, ten different formulations were synthesized.
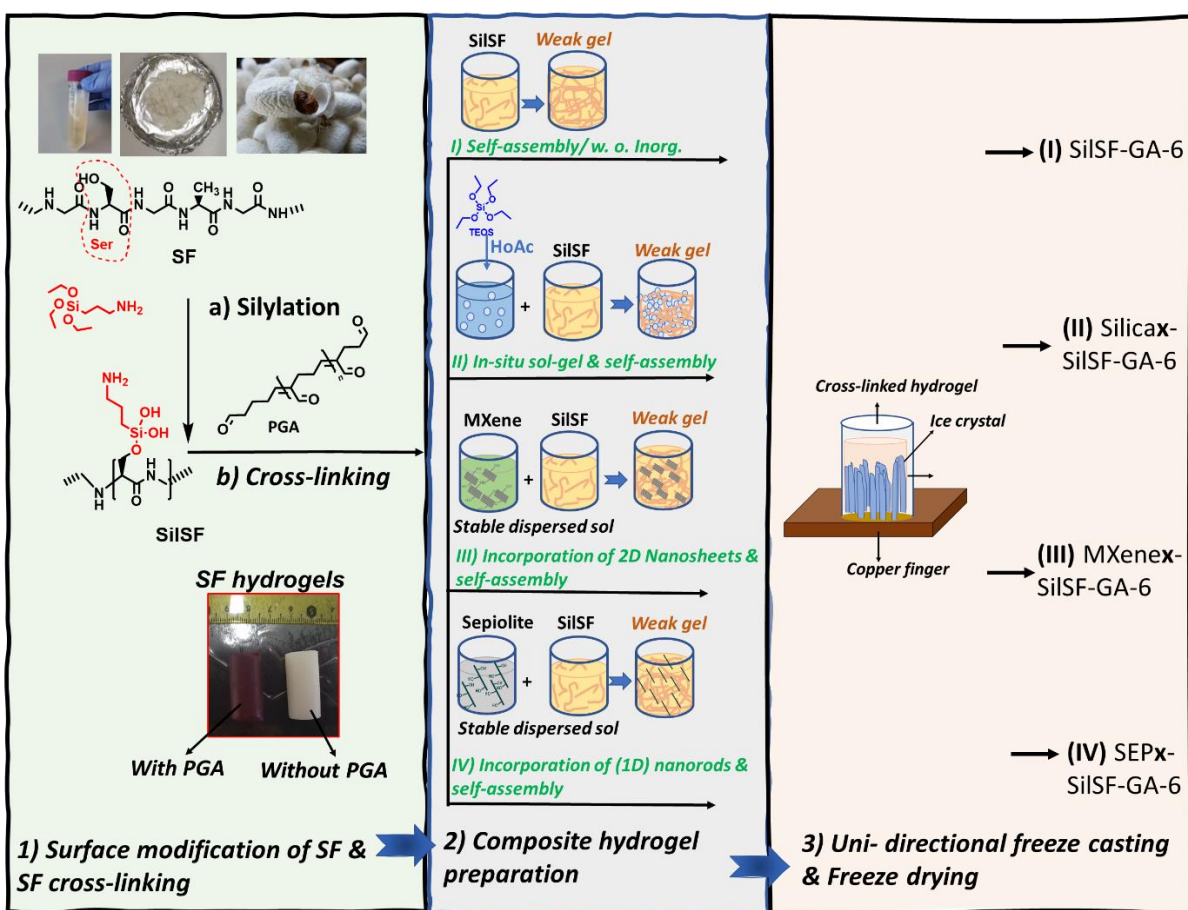

Figure 2. Scheme of the synthesis of the aerogel composites I) SilSF-GA-6, II) Silica**x**-SilSF-GA-6, III) MXene**x**-SilSF-GA-6, IV) SEP**x**-SilSF-GA-6.

The synthesis is briefly described as follows:

6

Synthesis of glutaraldehyde cross-linked silk fibroin (SilSF-GA-1, 6, &12). For SilSF-GA-6 (Table 1), the extracted silk fibroin (4ml, 40 mg/ ml) solution was modified with amino propyltriethoxysilane (APTES, 0.13 mL, 0.51 mmol) to prepare amino-modified silane silk fibroin (SilSF) at room temperature (ca. 23 °C) for 30 minutes. Then, the obtained SilSF solution was dialyzed against the distilled water to wash the unreacted APTES for 2 hours at room temperature. Next, 4 mL of purified SilSF solution was cross-linked with glutaraldehyde as the cross-linking agent (25 v/v%, 0.12 mL) at room temperature. The solution's color changed from white to dark orange and then purple within several minutes of stirring at room temperature. Afterward, acetic acid (HOAc, 0.5 mL, 120 mM) was added, and the solution was cast in polypropylene cylindrical moulds to complete the gelation in a ventilation oven (60 °C, 12 h). After the onset of gelation, the obtained hydrogel was processed by uni-directional freeze casting, according to our previous method[27] as well as taking the Nishihara *et al.*[28] modified procedure into account. Thus freeze-casting was performed by freezing the wet hydrogels uni-directionally at a constant rate by placing the hydrogels on top of a cold copper surface in direct contact with liquid nitrogen (-196 °C). The ice growth was initiated from the bottom of the tube and continued until the sample was completely frozen. Afterward, the sample was transferred into a freeze-drier and dried at -55 °C and 0.04 mbar for 2-10 days, depending on the size of the monoliths.

Table 1. List of aerogel formulations with information on their composition and synthesis conditions

Formulations[a]	SilSF (mg/mL)	(Inorg.), ceramic	GA[b], [GA]/ [NH$_2$]	Inorg./ Org.[c]	Gelation temperature (°C)	Gelation time (h)
SilSF-GA-6 (refers to X-*AeroSF*)	40	0	6	0	60	12
Silica3-SilSF-GA-1	40	Silica	1	3	60	0.5
Silica3-SilSF-GA-6	40	Silica	6	3	60	0.5
Silica3-SilSF-GA-12	40	Silica	12	3	60	0.5
Silica1.5-SilSF-GA-6	40	Silica	6	1.5	60	0.5
MXene0.01-SilSF-GA-6	40	MXene	6	0.01	60	8
MXene0.04-SilSF-GA-6	40	MXene	6	0.04	60	8
MXene0.1-SilSF-GA-6	40	MXene	6	0.1	60	8
SEP0.1-SilSF-GA-6	40	SEP	6	0.1	60	8
SEP0.06-SilSF-GA-6	40	SEP	6	0.06	60	8

a.   Selection of sample formulations
b.   GA content varied by the molar ratio of GA to surface amino (-NH$_2$) groups in SilSF.
c.   Mass fraction of inorganic to the organic moieties in the aerogel composites.

Fabrication of Silica$_x$ -SilSF-GA-6 hydrogel composites. For example typical Silica$_x$ with x=3 (Silica3) silylated silk fibroin (SilSF)-glutaraldehyde (GA)-6 aerogel composites (Silica3-SilSF-GA-6, see Table 1), firstly TEOS (3.37 mmol, 0.5 mL) was hydrolyzed at room temperature with acetic acid (HOAc, 0.5 mL, 120 mM) for 30 minutes. The hydrolyzed sol was added to the SilSF-GA-6 solution and CTAB (0.5 g) was then slowly added to the mixed solutions to avoid the phase separations. The solution was cast in polypropylene cylindrical and cubic mold to complete the gelation in a ventilation oven (60 °C, 30 min). After the onset of gelation, the as-prepared hydrogels were processed by uni-directional freeze-casting, according to the procedure mentioned above.

Fabrication of MXene & SEP-SilSF-GA-6 hydrogel composites. For a typical MXene0.04-SilSF-GA-6 aerogel composite in Table 1, the suspension of highly dispersed MXene (1mL, 5 mg/mL) in water was purged with Ar gas and allowed for ultra-sonication under Ar for 1 hour. Afterward, a highly dispersed MXene solution was added to the SilSF-GA-6 solutions, followed by the addition of HOAc (0.5 mL, 120 mM), casting, undirectional freeze-casting, and freeze-drying as stated previously. For typical SEP0.06-SilSF-GA-6, a highly dispersed sepiolite (1mL, 10 mg/ml) in water was added to the SilSF-GA-6 solution, followed by the addition of HOAc (0.5 mL, 120 mM), casting, undirectional freeze-casting, and freeze-drying.

3. Results and discussions

3.1. Chemical and crystalline structures

According to Fig. 2, the anisotropic composite aerogels were synthesized within four main steps. Despite most of the previously reported work dealing with anisotropic biopolymers and ceramic aerogels developed by directional freeze-casting the precursors' slurries, in this study, we are dealing with ice templating of hydrogels from a mixed solution of surface-modified SF and several inorganic nanoadditives. While silica nanostructure creates an interpenetrating network inside the self-assembled and cross-linked SF *via in-situ* sol-gel and self-assembly processes, 3D assembly of MXene and sepiolite inside the self-assembled SF was only directed through their colloidal dispersion and the nanostructuring process by freeze-casting. From several aspects, the hydrogelation before ice templating is advantageous. 1) Upon synergistic self-assembly and sol-gel reactions (only in the case of silica-based composites), dual interpenetrating network structures with nanoporosities beside macroposities were obtained. Thus, heat insulation performance is expected to be improved, and the nanoporosities will suppress the convection components of the heat transfer. 2) During the hydrogelation, the network slurries were frozen/trapped homogenously in the overall network structure. In contrast, slurries without gelation behaviour, are cryo-assembled by the ice front, and the constituents networks are built by thermally assisted phase separation.

Since the amino groups on the SF structure are very low, the surface chemistry of SF was firstly modified with amino-modified silanes (APTES). The condensation of various organosilanes with SF has been thoroughly studied in our previous works[19, 15]. Nevertheless, the addition of APTES to SF polymer was substantiated by the ATRFT-IR spectrum indicated in Fig. SI 1, with assigned peaks of Si-O-C at 987-1121 cm^{-1}. Since SilSF after modification with silane was undergone to the dialysis and purification, the Si-O-C peaks were attributed to the covalent interactions between SF and APTES, not APTES itself. Next, the surface amino groups were targeted for reaction with GA as one of the most common cross-linker, with varying its concentration adapted to the available surface amine groups ([GA]/[Surface amines] molar ratio: 1, 6, and 12.

In the case of silica contained composites (Silica**x**-SilSF-GA-**y**), silica sol was developed from acid-catalyzed hydrolysis of tetra-functional silane, TEOS, and then added to the cross-linked SF. The overall solution's pH was finally around 4, which was sufficient for the formation of the dual network of the silica and the cross-linked SF in the oven at 60 °C. The gelation time was varied depending on the GA content and was shortened at higher concentrations. Once the hydrogels were formed, they were processed by uni-directional freeze-casting with a thermal gradient applied by a thermal contact of the hydrogels with a cooled surface in contact with liquid nitrogen. Subsequently, freeze-drying was used to obtain the anisotropic aerogel samples.

According to the ATR-FTIR spectra of Figure 3a and b, the interaction of silica with the organic network is substantiated by characteristic bands υ_{as} (-Si−O−C-) at 1145 cm^{-1} in the spectrum, supporting the presence of covalent linkages between SF and the silica phase. This is also confirmed with solid-state mas ^{1}HNMR spectroscopy with characteristic peaks (corresponds to (4) at Fig. 3e) at δ = 4.3 ppm, attributed to silanol groups' condensation with the hydroxyl side chain of SF. For all hybrid samples, the incorporation of nanostructured silica to the network is substantiated by the presence of characteristic bands υ_{as} (-Si−O−Si-) at 1100 cm^{-1} but also through solid-state MAS ^{29}Si NMR spectroscopy (Fig. 3d), with the presence of Q_n (TEOS condensations, n: number of siloxane bonds, -97 (Q_2) and -107 ppm (Q_3) and T_n associated with SF-APTES condensation (-64 ppm).

In all composites, the SilSF biopolymer part of the composite was characterized by amide I (υ_{as} (C=O), 1618−1640 cm^{-1}), amide II (δ_s (N−H) deformations/ bending 1512−1544 cm^{-1}), and amide III (υ_{as} (C−N) 1230 cm^{-1}) vibrations at Fig. 3a[19]. During the *in situ* sol−gel processing of silanes and SilSF self-assembly, the randomly oriented SF biopolymers undergo partial conformational changes to β-sheet secondary structures. The influence of secondary structure formation in the

peak position of the amide I band at the FT-IR spectrum was thoroughly discussed in our previous work[19].

In addition, the presence of amine groups in Silica**x**-SilSF can be reflected by the absorption peaks centered at about 3295 cm^{-1}, in Fig. 3b, which is reduced in the intensity with increasing the molar ratio of GA in the composites. This absorption band can also be overlapped with -OH stretching vibration from intra- /inter-molecular hydrogen-bonded hydroxyl groups at 3285 cm^{-1} belongs to the self-assembled SilSF moieties. In addition, the amino-functionalization of SilSF was further confirmed with the presence of T_2 peaks at 64 ppm assigning to the two (-Si-O-Si-) bonds. Upon cross-linking of Silica**x**-SilSF with condensate product of GA, poly glutaraldehyde (PGA), two different double bonds appear in the structure of SilSF-GA, *i.e.*, -C=C- bonds from the PGA, and -C=N- from the cross-linking reaction between the amine groups in SilSF and aldehyde groups in the PGA. These double bonds form a conjugated planar structure in the SilSF-GA, enabling it to become autofluorescent, as it is also evident from its dark purple color of hydrogels shown in Fig. 2. The peak at 1658 cm^{-1} is attributed to the imine bond (-C=N-), and the peak at 1585 cm^{-1} is associated with the -C=C- bond. Nevertheless, the amine functional groups of SilSF and GA cross-linking are hardly detectable or hidden by SF peaks because the molecular weights of GA and APTES are much smaller than that of SF. The imine bond (5) has better confirmed at δ = 7.4 ppm at solid-state MAS ^{1}H NMR spectroscopy in Fig. 3e but also through CHNS elemental analysis in Fig. SI 2a. According to the CHNS elemental analysis, when more GA was added to the composite, the carbon and hydrogen percentage was also increased. Thermogravimetric analysis (TGA), as shown in Fig. SI 2b, indicates that the Silica**x**-SilSF-GA-**y** aerogel composite series was thermally stable up to ~ 230.6 °C. SF, the alkyl moiety in the SilSF (APTES), and GA decompose around 281.6 °C and 390.8 °C, respectively. Also, the different weight losses (wt %) and the overall rest masses of the hybrids confirmed the presence of SF and GA at the various loading extents. The designated characteristic peaks in the solid-state MAS ^{13}C NMR spectroscopy that belong to the carbon resonance in the Silica**x**-SilSF-GA-**y** aerogel composites confirm the proposed structure indicated in Fig. 3c.

In order to confirm the incorporation of MXene ($Ti_3C_2T_X$) 2D nanosheets into the aerogel matrix, X-ray diffraction (XRD), X-ray photoelectron (XPS), and FT-IR spectroscopy of the representative MXene0.1-SilSF-GA-6 (MXene/SilSF: 0.1) aerogel composites were studied.

MXenes represent a newly emerged family of two-dimensional (2D) materials obtained by leaching out the metal ions from transition metal carbides and nitrides with the general formula of $M_{n+1}X_nT_X$ (1≤n≤3), where M denotes a transition metal, *i.e.,* Ti, V, Mo, Sc, Nb, and X indicates carbon and/or

nitrogen, and T_X represents functional groups (OH, O, and/or F). MXenes are synthesized from etching out the A layer in the MAX phases, a class of layered ceramic with a general formula of $(M_{n+1}AX_n)$, using HF or from HF resulting precursors (e.g., LiF+HCl)[29].

According to the XRD pattern of Fig. 4a, MXene nanosheet was detected in the aerogel matrix through its most intense peak (002) at 9.0°, which was generated from the phase changes in its MAX phase (Ti_3AlC_2) though a selective Al layer etching. A peak shift from 9.5° (in MAX) to 9° (in MXene) belongs to the basal planes of (002) peak takes place due to the removal of Al in the Ti_3AlC_2 and incorporation of surface terminations as (T_x: -F, -O, -OH) in $Ti_3C_2T_x$[30]. Such surface termination groups enable MXene nano-dispersibility inside the SF solution but also its further dipole-dipole interactions and hydrogen bondings with surface termination at SF chains and subsequent homogeneous mixing at nanoscale before hydrogelation to occur. This was also confirmed with the XPS survey spectrum, indicating all the elemental composition but also valence states of the MXene in the MXene-SilSF-GA-6 matrix. The Ti 2p spectrum (Fig. 4b), which is located at 455.0 eV and 456.2 eV, corresponding to Ti-C and Ti-X bonds, respectively. The C 1s peaks at 281.1 eV, and 284.6 eV correspond to the Ti-C and C-C bond of SilSF-GA, respectively. The O 1s peaks located at 529.8 eV and 531.8 eV corresponds to O 1s in SiO_2 and hydroxyl groups. In addition, the F 1s XPS shows an intense peak at 683.7 eV, attributed to Ti_3C_2F[31].

Incorporation of the fibrous structure of sepiolite nanorod into the SilSF-GA matrix was confirmed by FT-IR spectroscopy (Fig. 4c) with the presence of characteristic peaks correspond to -Mg-Si-O- (420 cm^{-1}) and -Si-O-Si- (1060 cm^{-1}) besides those peaks belong to the organic components of composites. In addition, the diffraction spectrum of SEP**x**-SilSF-GA-6 at Fig. 4d indicates the peak at $2\theta = 7.4°$ (110), which is a characteristic of the lattice structure of sepiolite minerals[22].
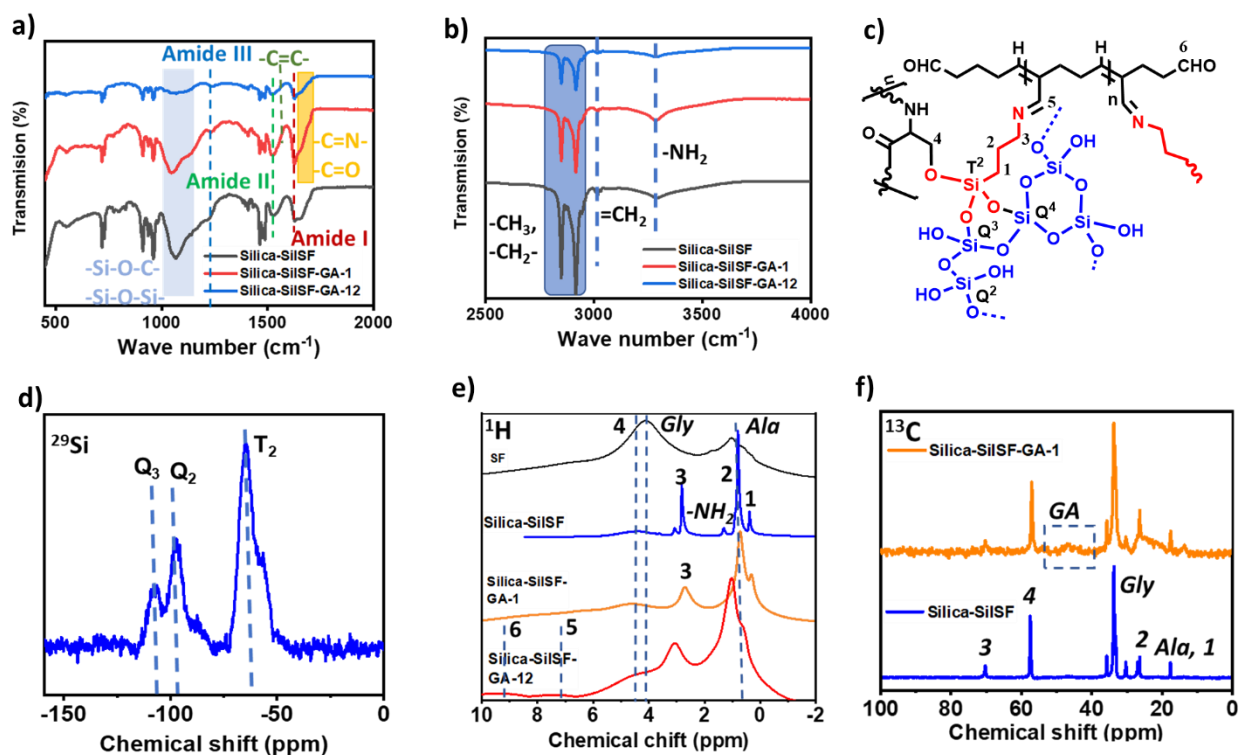
Figure 3. a) and b) ATRFT-IR spectra of Silica**x**-SilSF-GA-**y** composite aerogels c) proposed molecular structure of Silica**x**-SilSF-GA-**y** composite aerogels with corresponding d) solid-state MAS ^{29}Si e) ^{1}H, and f)^{13}C NMR spectra of Silicax -SilSF-GA-y composite aerogels.
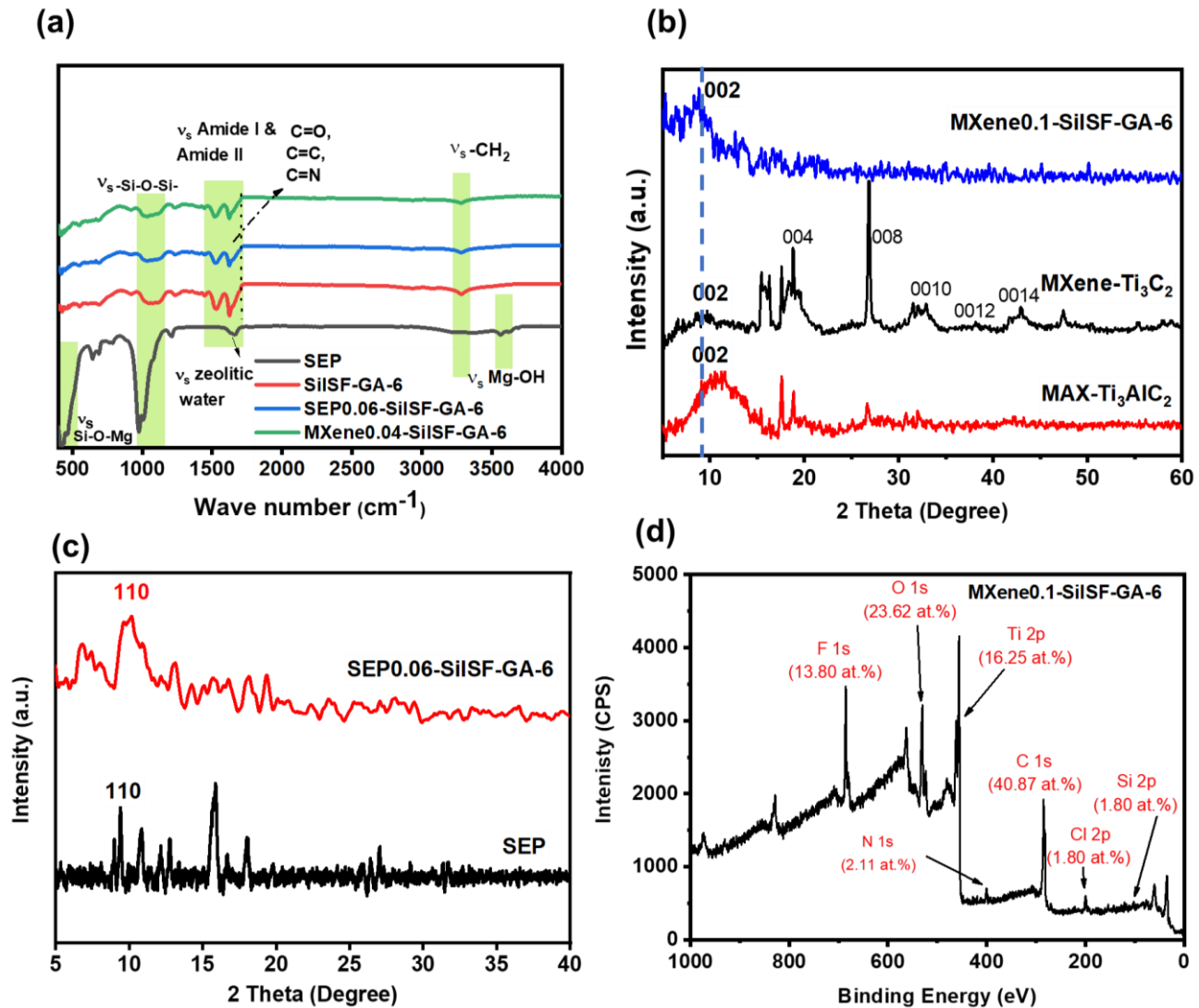
Figure 4. a) XRD, b) XPS of MXene0.1-SilSF-GA-6 composite aerogels, c) ATR FT-IR spectra, and I) XRD pattern of SEP-0.06-SilSF-GA composite aerogels.

3.2. Physical and microstructural analyses

According to the processing steps shown in Fig. 2, the Silica**x**-SilSF-GA-**y** hybrid hydrogels, which were freshly gelled and had enough amount of the solid phase, were frozen unidirectionally under a pseudo-steady-state of ice growth condition, an array of phase-separated polygonal ice rods grow in parallel with the freezing direction from the bottom of the hydrogel. This strategy produced frozen gels consisting of anisotropic ice crystals surrounded by the walls formed by the dispersed silica network and SilSF polymers, which were previously cross-linked by GA. After removing the ice template from the gel by freeze-drying, monolithic aerogels with a hierarchically organized porous structure comprising micro and mesopore as a result of concomitant sol-gel and self-assembly process and

13

ordered macropores, as a result of ice templating, were obtained. The internal microstructural pattern, from a multiscale standpoint, was studied with a combination of scanning electron microscopy (SEM), transmission electron microscopy (TEM), and X-ray micro and nano-computed tomography (micro and nano-CT). The SEM micrographs revealed aligned lamella-shaped channels for Silica3-SilSF-GA-1 (Fig. 5b) having diameters between 15 and 18 μm (measured by ImageJ) and a cell wall thickness between 0.4 and 1.5 μm, which by itself consists of fibrous cross-linked SF and micro and mesoporous silica networks – (Fig 5c). This sample's microstructure also consists of pearl necklace morphologies, which is a typical structure for silica and silica aerogels composites (Fig. 5d)[32]. In addition, the uniform distribution of all key network elements Si, C, N, and O, as observed with TEM-EDX elemental mapping, substantiates the homogenous hybridization at the nanoscale (Fig. SI 3). The composites' microstructural pattern with 6 and 12 molar content of GA in Fig. 5 f-h also indicate highly aligned pore channels. However, by increasing the GA content, the bridge structures across the pore channels with thicker network struts appear, leading the overall structure to resemble the cuttlefish bone's microstructure (Fig. 5 e). The lamella and bridge microstructural arrangement for sample Silica3-SilSF-GA-6 was also evident from the micro-nano-CT analysis, as indicated in Fig. 6a, b, and c. The recorded nano-CT at Figure 6c reveals the anisotropic pore channel alignment in the parallel direction of the ice crystal growth and created cross-bridges between the lamellae at lower length scales.

The same aligned structures with the lamella-bridge micromorphologies were also seen in MXene**x**-SilSF-GA-6 (*cf.* Fig. 5 i-l, Fig. SI 4) and SEP**x**-SilSF-GA-6 (*cf.* Fig. 5 m-p) in which SilSF-GA intertwined with the nanostructures of SEP nanorods and MXene nanosheets. Since MXene nanosheets have a layered structure in the length scale of a few tenths of microns (~20 μm)[30], the network feature size of resulting aerogel composites was also much larger (ca. 100-250 μm) than that of the Silica-SilSF-GA composites (<20 μm). The same nanoporous morphologies were also seen in both cases as the nanoporosity is an intrinsic feature of the self-assembled SilSF. In SEP-SilSA-GA-6, pore channel diameter is relatively smaller (50-100 μm) than that of MXene, as the SEP nanorods have also better nanodispersibility in SF matrix compared to MXene due to the smaller size of SEP nanorods (*ca.* 1-5 μm). The homogenouse distribuation of all elements including Ti have also been confimed by SEM-EDX elemental mapping shown at Fig.SI 4.
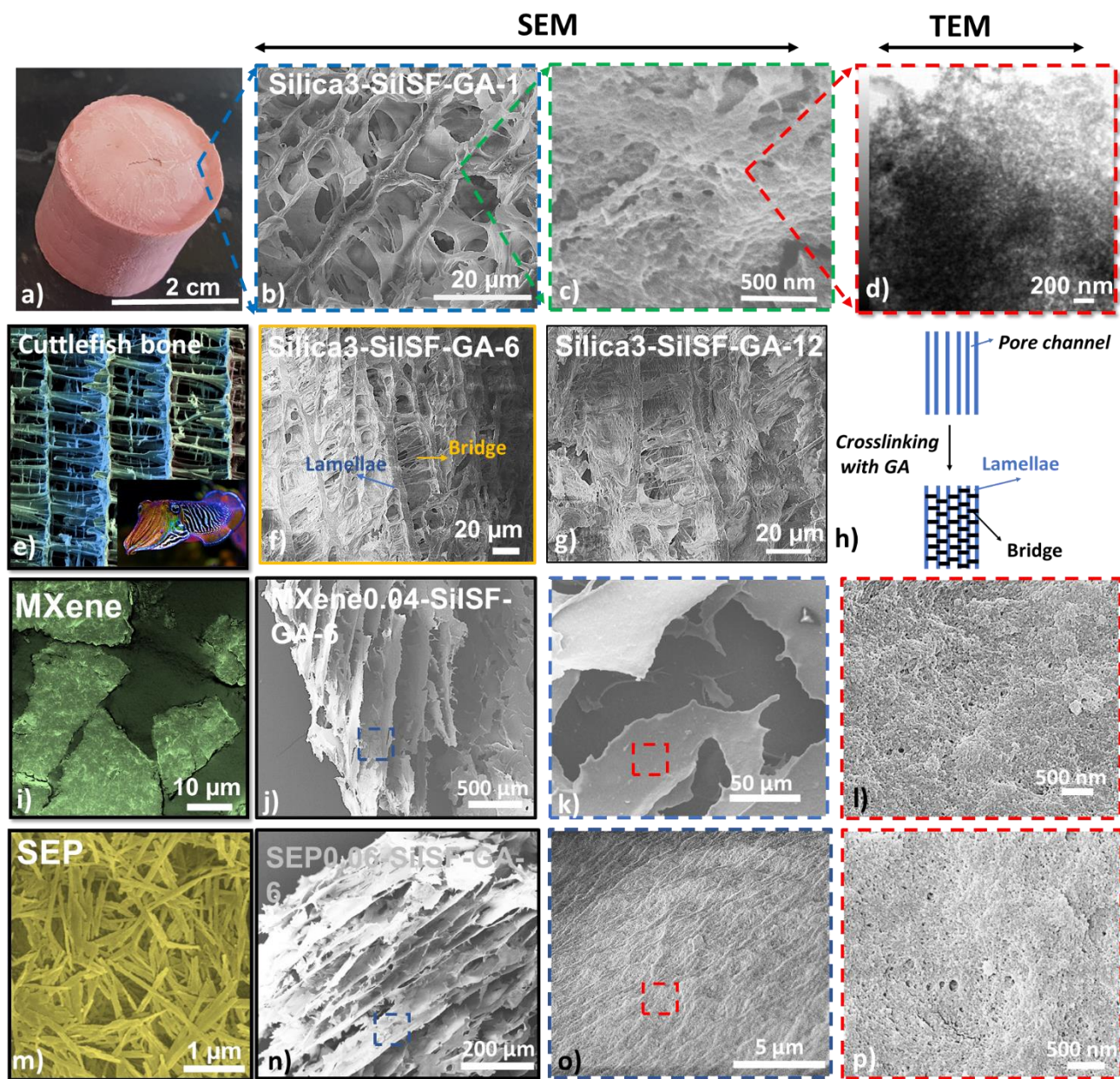
Figure 5. A multiscale view of the porous microstructures. a) a digital image of Silica-3-SilSF-GA-1; b) and c) SEM micrographs of structure in alignment with pore channel at different magnifications, d) TEM micrograph of Silica3-SilSF-GA-1; e) the cuttlefish bone microstructure, with permission from Ref. [33], f) SEM micrographs of Silica-3-SilSF-GA-6, and g) SEM micrographs of Silica-3-SilSF-GA-12 which resemble h) the lamellae and bridge structure in the cuttlefish bone upon increasing the GA content; i-l) SEM micrographs of MXene NSs and MXene0.04-SilSF-GA-6 at different magnifications; m-p) SEM micrographs of Sepiolite nanorods and SEP-0.06-SilSF-GA-6 aerogel at different magnifications.

In the case of Silica**x**-SilSF-GA-**y** aerogel composites, in order to conduct concomitant sol-gel and self-assembly in the silane and SilSF, phase separation was avoided between the generated silicate species and the aqueous solution of SF. As it was indicated in previous studies[19], the macroscopic phase separation can be easily prevented by adding a cationic surfactant like CTAB to increase the

miscibility of both organic and silane phases at molecular scales. Even though, after hydrogelation and freeze-casting, CTAB was washed out, it was hypothesized that the complete removal of a trace amount of the CTAB might be unavoidable in this process. The same hypothesis was also given in the previously reported silica and silsesquioxane based hybrid aerogels using CTAB as phase separation suppressing agents.[32, 18] This could result in nanopores' collapse but also a decrease in nitrogen gas adsorption performance (Fig. 7a) and specific surface area (S_{BET}=14 m^2 g^{-1}) compared to the MXene (S_{BET}=66 m^2 g^{-1}) and SEP-SilSF-GA (S_{BET}=60 m^2 g^{-1}) aerogel composite counterparts without using CTAB in the gelation process (Fig. 7g). MXene and SEP nanosheets alone contain high specific surface area due to their intrinsic nanopore and nanolayered structures; thus, the resulted composites from them have also indicated a slightly higher surface area. Nevertheless, all the composites have shown the Knudsen effect as their mesopore diameters are far below 70 nm, the mean free path of the air molecules, to suppress the gaseous thermal conductivity (Fig. 7b, and h). Also, N_2 adsorption-desorption isotherms (Fig. 7a and b) were according to type IV isotherm of IUPAC classification with H_1 hysteresis loop type, with capillary condensation occurring at $p/p_0 > 0.5$, confirming that almost all hybrids also have a mesoporous character with an open-ended cylindrical pore morphology[34].
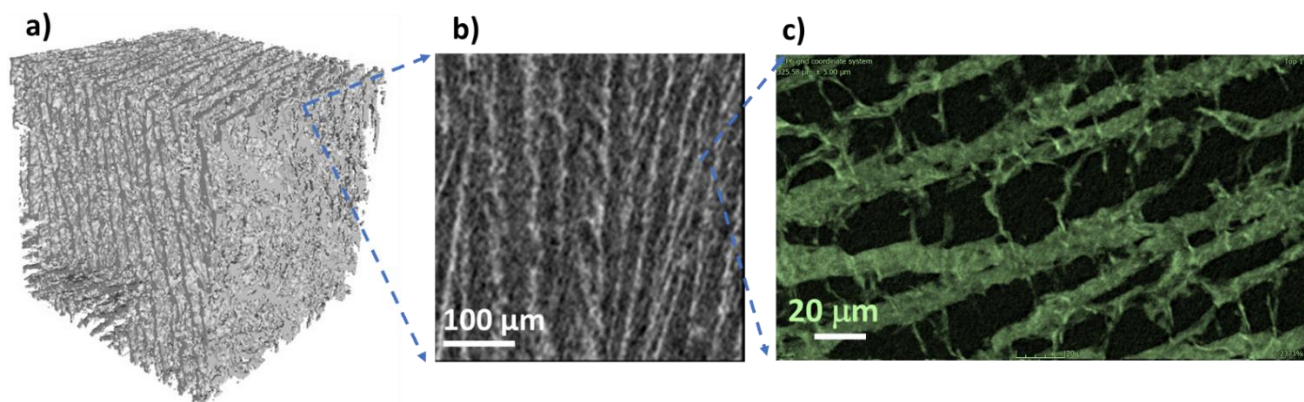

Figure 6. 3D reconstructions of the porous structure in sample Silica3-SilSF-GA-6 nanocomposite derived from X-ray microtomography, which show the alignment of the porous structure in the line of ice growth direction and b) X-ray nanotomography image is showing the pore and microstructure micromorphology, and c) a high magnification view from cuttlefish bone mimetic bridge and lamellae structure.

In comparison to the silica and silsesquioxane silk fibroin aerogel hybrids, the overall bulk density (ρ_b) of the composite aerogels (Fig. 7 c-f) was very low (*e.g.,* ρ_b < 0.1 g cm^{-3}). The increase of the glutaraldehyde concentration was leading to an increased bulk density of the aerogel composite due to the loading of a high mass to the overall aerogel composites. The same also was seen with increasing the silica content as the pore volume was decreased. Besides high surface areas, smaller mesopore diameters, the MXene and SEP contained aerogel composites demonstrated very low bulk densities of 0.06 g cm^{-3} and 0.058 g cm^{-3}, respectively in comparison to the silica-based composite with ρ_b=0.073 g cm^{-3}.
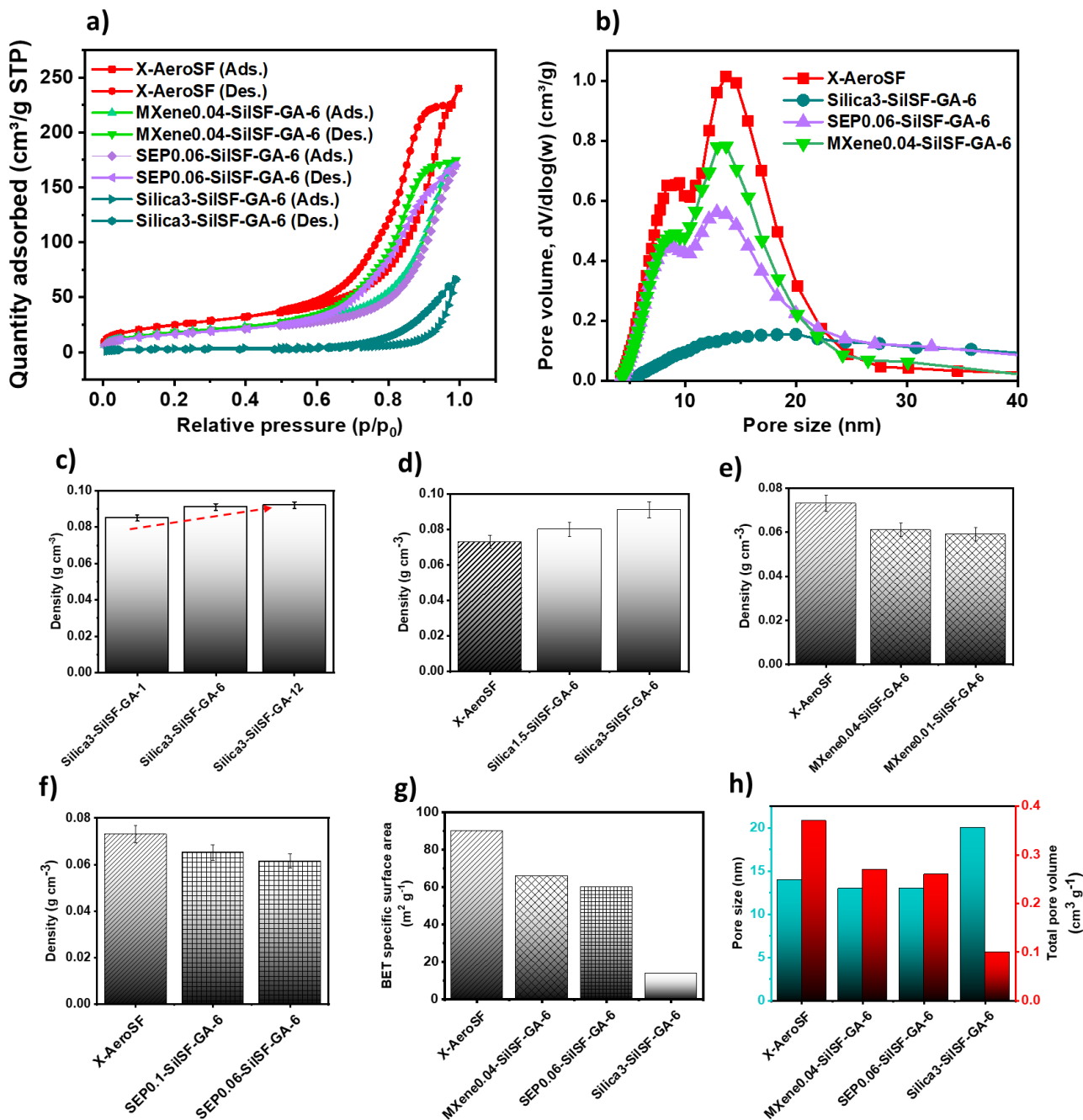
Figure 7. a) The N$_2$ adsorption-desorption isotherms, b) BJH pore size distribution of representative samples; c), d, e, and f) bulk density variations in aerogel composites, g) BET specific surface area, and h) pore size and, and pore volume variations in representative samples.

4.3. Thermal conductivity, anisotropic heat transfer behavior, fire resistivity in composite aerogels

Due to the low densities, high mesopore volume, and hierarchical porous character with mesopore size below the mean free path of the air (70 nm, Knudsen effect) (*cf.* Fig. 7h), aerogel composites of

the current study have shown an interesting thermal insulation performance with $\Lambda_{t, \text{II}}$ = 0.035-0.042W m^{-1}K^{-1} (*cf.* Fig. 8a). The thermal conductivity was measured in a parallel direction ($_\text{II}$) with respect to the ice crystal growth and pore lamella. Even though the macropore channel sizes in all composites were significantly larger compared to those in isotropic and supercritical dried silica and silsesquioxane-silk fibroin aerogels, the obtained thermal conductivity is still nearly in the same range. With the addition of secondary inorganic components of silica, Silica3-SilSF-GA-6 ($\Lambda_{t, \text{II}}$ = 0.035 W m^{-1}K^{-1}) and sepiolite, SEP0.06-SilSF-GA-6 ($\Lambda_{t, \text{II}}$ = 0.038 W m^{-1}K^{-1}) to the composite, the thermal conductivity was improved compared to the unmodified SilSF-GA ($\Lambda_{t, \text{II}}$ = 0.04 W m^{-1}K^{-1}). This is attributed to the numerous interfacial resistances between the aerogels' different components in their pore cell walls and the phonon scattering by these minerals in the composites. In order to have a better view on the heat transfer behavior of aerogel specimen in both transverse and longitudinal directions with respect to the pore channel direction, the dynamic temperature distribution of the Silica-3-SilSF-GA-6 cubic aerogels upon heating and monitoring by the infrared camera was studied. As shown in Fig. 8b and c, upon heating the sample in a longitudinal (18 mm thickness) or parallel direction to the pore channels, a gradient distribution of the temperature from the heating plate (64 °C) to the top surface of the aerogel was observed. Therefore, during 120 s, the top surface temperature was raised from 27.5 °C to 30.7 °C. However, upon heating the samples in a transverse or a perpendicular direction to the pore channel, the temperature of the aerogel sample's top surface after 120 s remained relatively constant at 29.9 °C. Thus, this observation substantiates the anisotropy in the pore morphology and subsequent anisotropy in the heat transfer behavior, allowing the heat to spread along the lamella direction and prevents heat localization upon the accumulation of thermal energy in the sample[14]. These results indicate that Silica3-SilSF-GA-6 aerogel composites are expected to act as anisotropic heat insulation material with potential thermal energy management applications.
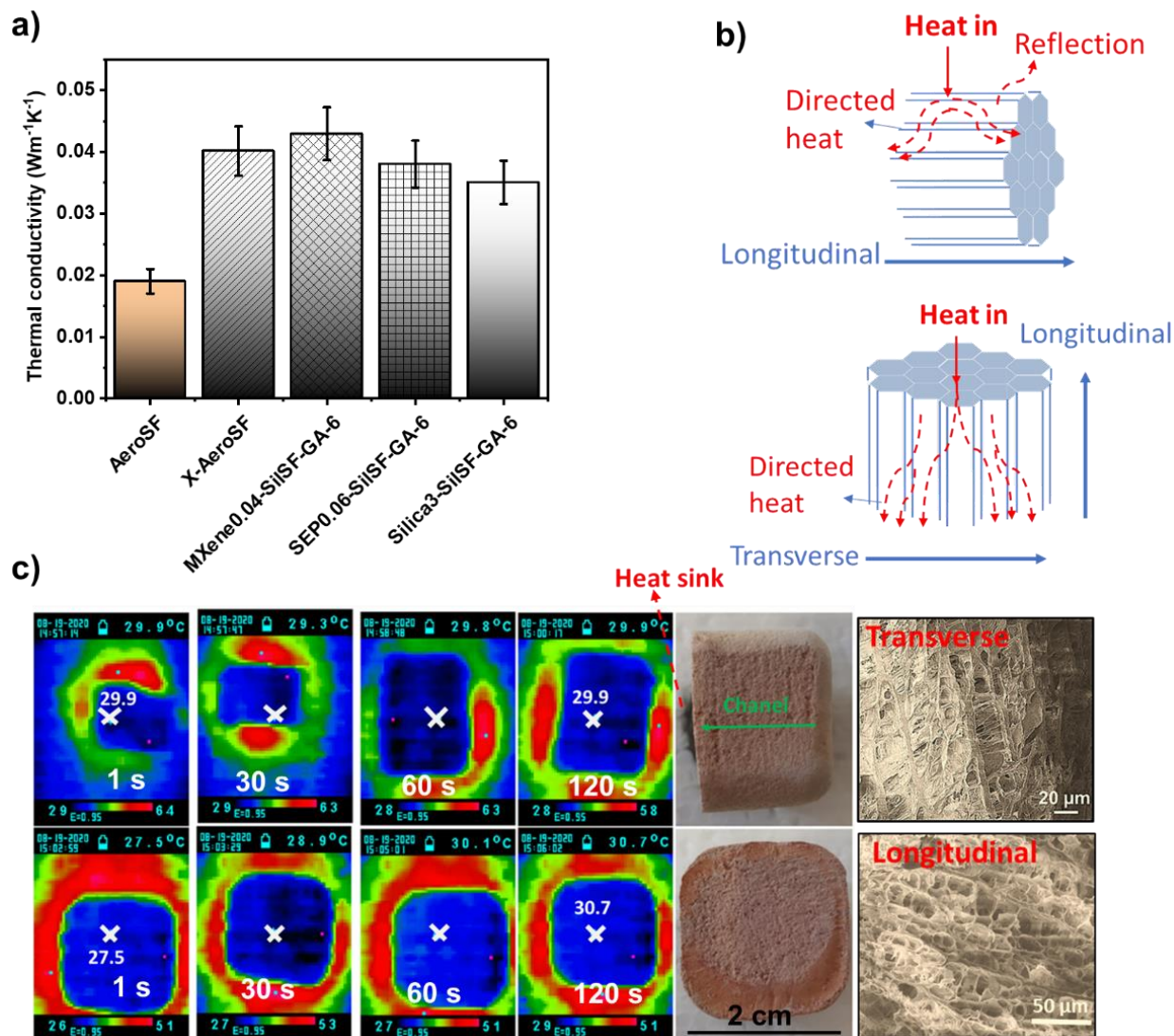
Figure 8. a) Thermal conductivity of some representative aerogel composite samples, b) scheme of expected heat transfer behavior in both transverse and longitudinal directions of anisotropic aerogel composite samples, c) thermal camera images of anisotropic Silica-3-SilSF-GA-6 sample to record the heat transfer on the sample surface during heating with a heat sink in both, transverse and longitudinal, directions and SEM images of the corresponding microstructure.

The other asset of the composite aerogels reported in this study is their thermal stability. This is evident from TGA-DSC curves (Fig. 9a), where three different thermal transitions at 240, 329, and 486 °C are associated with SF' s decomposition, aminopropyl moieties of APTES, and GA, respectively. It was also shown that the incorporation of the nano-additives silica, SEP, and MXene into the composite only influenced the rest mass after full decomposition without changing in the onset of decomposition of organic moieties. The rest mass of the aerogel composites was increased upon the incorporation of various amounts - measured value shown in brackets - of SEP (21.47%) and MXene (20.1%) compared to the reference SilSF-GA-6 (16.4%). Since APTES was used for amino

functionalization/silylation of SF (SilSF), its condensation reaction can form a silica network structure inside the aerogel matrix. By subtracting the silica mass resulted from the condensation of SilSF for all composites, the remaining rest masses indicate the SEP (5.07%) and MXene (3.7%) contributions, which are almost in agreement with their theoretical values in SEP (6%) and MXene (4%) in the composites reported at Table 1. The slight difference in theoretical and experimental values is due to the fact that small parts of these minerals have undergone precipitations during the gelation and therefore were not entirely incorporated into the composites.

Thanks to the nano-additives based on ceramic minerals having high intrinsic temperature stability incorporated into the aerogel composite, all aerogels showed heat resistivity during the burning test (*cf.* Figure 9b and c) without self-propagation of flame. After the burning test, the sample compositions in both bulk and crust sections of burnt samples were investigated using FT-IR spectroscopy (Fig. 9b). The bulk sections of the burnt area for all representative samples were remained intact, which was evident from the presence of amide I (υ_{as} (C=O), 1618−1640 cm^{-1}), and amide II (δ_s (N−H) deformation/ bending 1512−1544 cm^{-1}) (See Fig. 3a too). However, in the case of SEP contained composites, the crust section of the composite after burning showed a tendency to decompose and carbonize with remaining only inorganic parts. This implies that the MXene and interpenetrating silica network could confer a better fire-retardance effect on silk fibroin than the SEP.

A further asset of the uni-directional freeze-casting/ freeze drying approach, which was used to process the aerogel composites in the present work, is its versatility and adaptability for the preparation of various sample sizes and geometries. Suitable sample moldings and potential drying systems are selected to produce anisotropy during freeze-casting and to dry the samples (cf. Fig. 9d) entirely. This processing technique enables control of the sample's micro-morphologies upon controlling the ice crystal growth behavior and offers simplicity and versatility for fabricating various macrostructure with different building blocks or initial precursors[25].
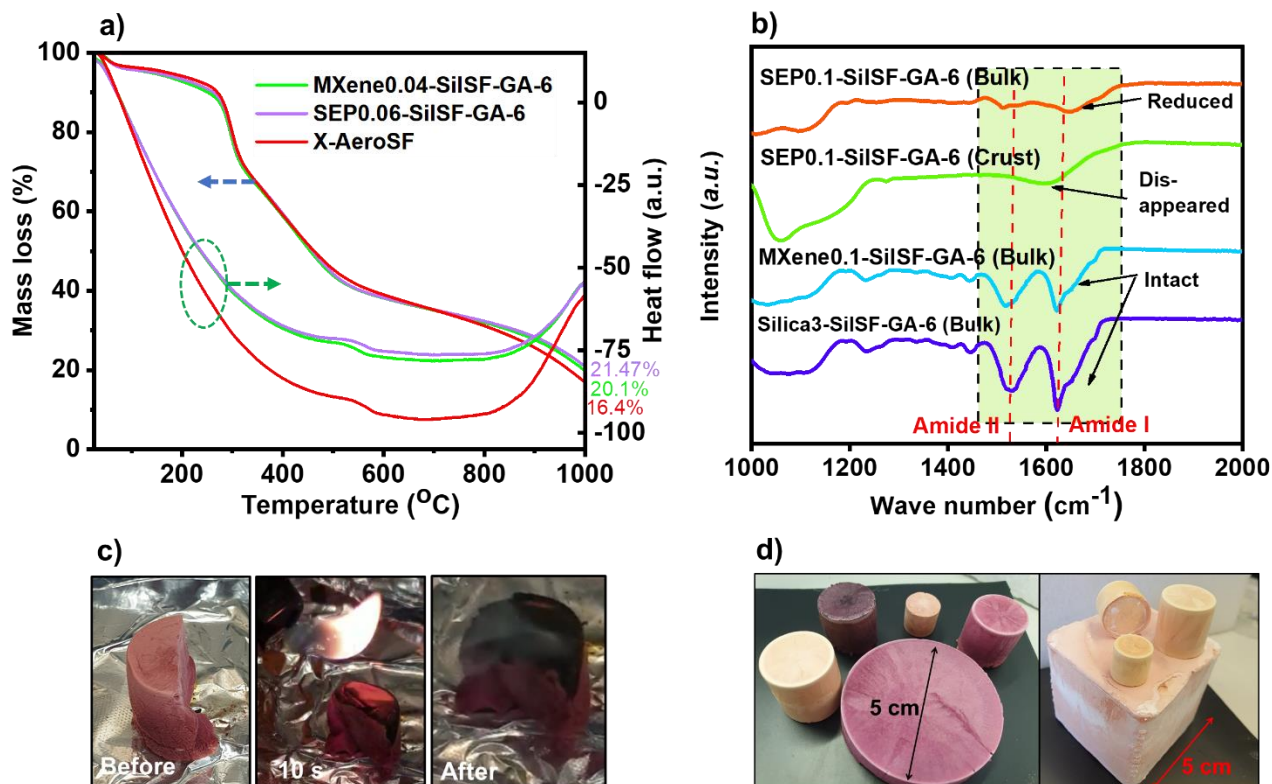
Figure 9 a) TGA-DSC analysis, b) ATR-FT-IR analysis of samples after burning, c) SEP-0.1-SilSF-GA-6 samples before, during, and after burning, and d) processability of aerogels' samples to different geometries and sizes.

5. Conclusions

A series of novel and anisotropic, fire-retardant silk fibroin-based aerogel composites were developed as anisotropic thermal insulators for a potential thermal energy management application. Exploiting from chemical modification and cross-linking of SF biopolymer with glutaraldehyde and incorporating various ceramic secondary phases such as SEP nanorods, MXene nanosheets, and interpenetrating silica nanostructures, together with the utilization of versatile uni-directional freeze-casting and -drying of the resulting hydrogels, aerogel macrostructures with interesting cuttlefish bone mimetic microstructures were developed. The synthesis condition has been thoroughly optimized for glutaraldehyde and ceramic contents to form composite hydrogels that are anisotropic structured by a later uni-directional freeze-casting step to control its microstructure and assemble the pore network into the desired directions and morphologies.

Besides lamella and bridge macro-pore morphologies obtained by uni-directional freeze-casting, the developed Silica**x**-SilSF-GA-**y** hybrid aerogels also indicated mesopore characters that originated from concomitant occurring of the sol-gel reaction and self-assembly in the silica and the SF biopolymer in the network, respectively. This was also observed in the MXene, and SEP containing aerogel

composites even though the macrostructure and macropore sizes in these composites were relatively larger. Overall, the hierarchical porosity, low densities (ρ_b=0.059-0.09 g cm^{-3}), and the anisotropic alignment of the pore channel resulted in excellent thermal insulation performance (λ_t=0.035-0.042 W m^{-1}K^{-1}) showing anisotropy in the heat transfer behavior. Altogether, the proposed biomimetic fire-resistive aerogel composites show a large potential for thermal energy management in energy-efficient buildings, space applications, and electrical device insulations.

Supporting Information (SI)

SI contains information regarding the used characterization methods but also some analytical results such as ATR FTIR spectrum of SilSF, CHN elemental analysis of Silicax-SilSF-GA-y, b) TGA analysis of Silicax-SilSF-GA-y, EDX-TEM elemental mappings of Silicax-SilSF-GA-y, EDX-SEM elemental mappings of MXenex-SilSF-GA-y.

6. References

(1)   Rashidi, S.; Kashefi, M. H.; Kim, K. C.; Samimi-Abianeh, O. Potentials of Porous Materials for Energy Management in Heat Exchangers – A Comprehensive Review. *Appl. Energy* **2019**, *243*, 206–232. https://doi.org/10.1016/j.apenergy.2019.03.200.

(2)   Moore, A. L.; Shi, L. Emerging Challenges and Materials for Thermal Management of Electronics. *Mater. Today* **2014**, *17* (4), 163–174. https://doi.org/10.1016/j.mattod.2014.04.003.

(3)   Hüsing, N.; Schubert, U. Aerogels—Airy Materials: Chemistry, Structure, and Properties. *Angew. Chem. Int. Ed.* **1998**, *37* (1-2), 22–45. https://doi.org/10.1002/(SICI)1521-3773(19980202)37:1/2<22::AID-ANIE22>3.0.CO;2-I.

(4)   Montes, S.; Maleki, H. 12 - Aerogels and Their Applications. In *Colloidal Metal Oxide Nanoparticles*; Thomas, S., Tresa Sunny, A., Velayudhan, P., Eds.; Elsevier, 2020; pp 337–399. https://doi.org/10.1016/B978-0-12-813357-6.00015-2.

(5)   Koebel, M.; Rigacci, A.; Achard, P. Aerogel-Based Thermal Superinsulation: An Overview. *J. Sol-Gel Sci. Technol.* **2012**, *63* (3), 315–339. https://doi.org/10.1007/s10971-012-2792-9.

(6)   Rudaz, C.; Courson, R.; Bonnet, L.; Calas-Etienne, S.; Sallée, H.; Budtova, T. Aeropectin: Fully Biomass-Based Mechanically Strong and Thermal Superinsulating Aerogel. *Biomacromolecules* **2014**, *15* (6), 2188–2195. https://doi.org/10.1021/bm500345u.

(7)   Jaxel, J.; Markevicius, G.; Rigacci, A.; Budtova, T. Thermal Superinsulating Silica Aerogels Reinforced with Short Man-Made Cellulose Fibers. *Compos. Part Appl. Sci. Manuf.* **2017**, *103*, 113–121. https://doi.org/10.1016/j.compositesa.2017.09.018.

(8)   An, L.; Wang, J.; Petit, D.; Armstrong, J. N.; Hanson, K.; Hamilton, J.; Souza, M.; Zhao, D.; Li, C.; Liu, Y.; Huang, Y.; Hu, Y.; Li, Z.; Shao, Z.; Desjarlais, A. O.; Ren, S. An All-Ceramic, Anisotropic, and Flexible Aerogel Insulation Material. *Nano Lett.* **2020**, *20* (5), 3828–3835. https://doi.org/10.1021/acs.nanolett.0c00917.

(9)   Zhao, S.; Malfait, W. J.; Demilecamps, A.; Zhang, Y.; Brunner, S.; Huber, L.; Tingaut, P.; Rigacci, A.; Budtova, T.; Koebel, M. M. Strong, Thermally Superinsulating Biopolymer–Silica Aerogel Hybrids by Cogelation of Silicic Acid with Pectin. *Angew. Chem. Int. Ed.* **2015**, *54* (48), 14282–14286. https://doi.org/10.1002/anie.201507328.

(10)   Song, M.; Jiang, J.; Qin, H.; Ren, X.; Jiang, F. Flexible and Super Thermal Insulating Cellulose Nanofibril/Emulsion Composite Aerogel with Quasi-Closed Pores. *ACS Appl. Mater. Interfaces* **2020**, *12* (40), 45363–45372. https://doi.org/10.1021/acsami.0c14091.

(11)   Shen, X.; Wang, Z.; Wu, Y.; Liu, X.; He, Y.-B.; Kim, J.-K. Multilayer Graphene Enables Higher Efficiency in Improving Thermal Conductivities of Graphene/Epoxy Composites. *Nano Lett.* **2016**, *16* (6), 3585–3593. https://doi.org/10.1021/acs.nanolett.6b00722.

(12)   Shahil, K. M. F.; Balandin, A. A. Graphene–Multilayer Graphene Nanocomposites as Highly Efficient Thermal Interface Materials. *Nano Lett.* **2012**, *12* (2), 861–867. https://doi.org/10.1021/nl203906r.

(13)   Shanyu Zhao, Wim J. Malfait, Natalia Guerrero-Alburquerque, Matthias M. Koebel, Gustav Nyström. Biopolymer Aerogels: Chemistry, Properties and Applications. *Angew. Chem. Int. Ed.* **2018**, *57*, 7580. https://doi.org/10.1002/ange.201709014.

(14)   Li, T.; Song, J.; Zhao, X.; Yang, Z.; Pastel, G.; Xu, S.; Jia, C.; Dai, J.; Chen, C.; Gong, A.; Jiang, F.; Yao, Y.; Fan, T.; Yang, B.; Wågberg, L.; Yang, R.; Hu, L. Anisotropic, Lightweight, Strong, and Super Thermally Insulating Nanowood with Naturally Aligned Nanocellulose. *Sci. Adv.* **2018**, *4* (3), eaar3724. https://doi.org/10.1126/sciadv.aar3724.

(15)   Wicklein, B.; Kocjan, A.; Salazar-Alvarez, G.; Carosio, F.; Camino, G.; Antonietti, M.; Bergström, L. Thermally Insulating and Fire-Retardant Lightweight Anisotropic Foams Based on Nanocellulose and Graphene Oxide. *Nat. Nanotechnol.* **2015**, *10* (3), 277–283. https://doi.org/10.1038/nnano.2014.248.

(16)   Qin, Y.; Peng, Q.; Zhu, Y.; Zhao, X.; Lin, Z.; He, X.; Li, Y. Lightweight, Mechanically Flexible and Thermally Superinsulating RGO/Polyimide Nanocomposite Foam with an Anisotropic Microstructure. *Nanoscale Adv.* **2019**, *1* (12), 4895–4903. https://doi.org/10.1039/C9NA00444K.

(17)   Rockwood, D. N.; Preda, R. C.; Yücel, T.; Wang, X.; Lovett, M. L.; Kaplan, D. L. Materials Fabrication from Bombyx Mori Silk Fibroin. *Nat. Protoc.* **2011**, *6* (10), 1612–1631. https://doi.org/10.1038/nprot.2011.379.

(18)   Maleki, H.; Whitmore, L.; Hüsing, N. Novel Multifunctional Polymethylsilsesquioxane–Silk Fibroin Aerogel Hybrids for Environmental and Thermal Insulation Applications. *J. Mater. Chem. A* **2018**, *6* (26), 12598–12612. https://doi.org/10.1039/C8TA02821D.

(19)   Maleki, H.; Montes, S.; Hayati-Roodbari, N.; Putz, F.; Huesing, N. Compressible, Thermally Insulating, and Fire Retardant Aerogels through Self-Assembling Silk Fibroin Biopolymers Inside a Silica Structure—An Approach towards 3D Printing of Aerogels. *ACS Appl. Mater. Interfaces* **2018**, *10* (26), 22718–22730. https://doi.org/10.1021/acsami.8b05856.

(20)   Bruder, V.; Ludwig, T.; Opitz, S.; Christoffels, R.; Fischer, T.; Maleki, H. Hierarchical Assembly of Surface Modified Silk Fibroin Biomass into Micro-, and Milli-Metric Hybrid Aerogels with Core-Shell, Janus, and Composite Configurations for Rapid Removal of Water Pollutants. *Adv. Mater. Interfaces* **2021**, *n/a* (n/a), 2001892. https://doi.org/10.1002/admi.202001892.- In press

(21)   Alhabeb, M.; Maleski, K.; Anasori, B.; Lelyukh, P.; Clark, L.; Sin, S.; Gogotsi, Y. Guidelines for Synthesis and Processing of Two-Dimensional Titanium Carbide (Ti3C2Tx MXene). *Chem. Mater.* **2017**, *29* (18), 7633–7644. https://doi.org/10.1021/acs.chemmater.7b02847.

(22)   Tang, Q.; Wang, F.; Tang, M.; Liang, J.; Ren, C. Study on Pore Distribution and Formation Rule of Sepiolite Mineral Nanomaterials. *J. Nanomater.* **2012**, *2012*, 382603. https://doi.org/10.1155/2012/382603.

(23)   Seol, J. H.; Jo, I.; Moore, A. L.; Lindsay, L.; Aitken, Z. H.; Pettes, M. T.; Li, X.; Yao, Z.; Huang, R.; Broido, D.; Mingo, N.; Ruoff, R. S.; Shi, L. Two-Dimensional Phonon Transport in Supported Graphene. *Science* **2010**, *328* (5975), 213. https://doi.org/10.1126/science.1184014.

(24)   Shao, G.; Hanaor, D. A. H.; Shen, X.; Gurlo, A. Freeze Casting: From Low-Dimensional Building Blocks to Aligned Porous Structures—A Review of Novel Materials, Methods, and Applications. *Adv. Mater.* **2020**, *32* (17), 1907176. https://doi.org/10.1002/adma.201907176.

(25)   Shahbazi, M.-A.; Ghalkhani, M.; Maleki, H. Directional Freeze-Casting: A Bioinspired Method to Assemble Multifunctional Aligned Porous Structures for Advanced Applications. *Adv. Eng. Mater.* **2020**, *22* (7), 2000033. https://doi.org/10.1002/adem.202000033.

(26)   Zheng Z, Guo S, Liu Y, Wu J, Li G, Liu M, Wang X, Kaplan D. Lithium-Free Processing of Silk Fibroin. *J Biomater Appl* **2016**, *31(3)*, 450–463. https://doi.org/10.1177/0885328216653259.

(27)   Maleki, H.; Shahbazi, M.-A.; Montes, S.; Hosseini, S. H.; Eskandari, M. R.; Zaunschirm, S.; Verwanger, T.; Mathur, S.; Milow, B.; Krammer, B.; Hüsing, N. Mechanically Strong Silica-Silk Fibroin Bioaerogel: A Hybrid Scaffold with Ordered Honeycomb Micromorphology and Multiscale Porosity for Bone Regeneration. *ACS Appl. Mater. Interfaces* **2019**, *11* (19), 17256–17269. https://doi.org/10.1021/acsami.9b04283.

(28)   Nishihara, H.; Mukai, S. R.; Yamashita, D.; Tamon, H. Ordered Macroporous Silica by Ice Templating. *Chem. Mater.* **2005**, *17* (3), 683–689. https://doi.org/10.1021/cm048725f.

(29)   Naguib, M.; Mashtalir, O.; Carle, J.; Presser, V.; Lu, J.; Hultman, L.; Gogotsi, Y.; Barsoum, M. W. Two-Dimensional Transition Metal Carbides. *ACS Nano* **2012**, *6* (2), 1322–1331. https://doi.org/10.1021/nn204153h.

(30)   Dong, Y.; Wu, Z.-S.; Zheng, S.; Wang, X.; Qin, J.; Wang, S.; Shi, X.; Bao, X. Ti3C2 MXene-Derived Sodium/Potassium Titanate Nanoribbons for High-Performance Sodium/Potassium Ion Batteries with Enhanced Capacities. *ACS Nano* **2017**, *11* (5), 4792–4800. https://doi.org/10.1021/acsnano.7b01165.

(31)   Xia, Q. X.; Fu, J.; Yun, J. M.; Mane, R. S.; Kim, K. H. High Volumetric Energy Density Annealed-MXene-Nickel Oxide/MXene Asymmetric Supercapacitor. *RSC Adv.* **2017**, *7* (18), 11000–11011. https://doi.org/10.1039/C6RA27880A.

(32)   Kanamori, K.; Aizawa, M.; Nakanishi, K.; Hanada, T. New Transparent Methylsilsesquioxane Aerogels and Xerogels with Improved Mechanical Properties. *Adv. Mater.* **2007**, *19* (12), 1589–1593. https://doi.org/10.1002/adma.200602457.

(33)   Rocha, J. H. G.; Lemos, A. F.; Agathopoulos, S.; Valério, P.; Kannan, S.; Oktar, F. N.; Ferreira, J. M. F. Scaffolds for Bone Restoration from Cuttlefish. *Bone* **2005**, *37* (6), 850–857. https://doi.org/10.1016/j.bone.2005.06.018.

(34)   Horikawa, T.; Do, D. D.; Nicholson, D. Capillary Condensation of Adsorbates in Porous Materials. *Adv. Colloid Interface Sci.* **2011**, *169* (1), 40–58. https://doi.org/10.1016/j.cis.2011.08.003.